Structure reconstruction with Ewald sphere curvature considerations

2007 J. Phys.: Condens. Matter 19 216215

(http://iopscience.iop.org/0953-8984/19/21/216215)

IOP PUBLISHING JOURNAL OF PHYSICS: CONDENSED MATTER

J. Phys.: Condens. Matter **19** (2007) 216215 (10pp) doi:10.1088/0953-8984/19/21/216215

Structure reconstruction with Ewald sphere curvature considerations

Ning Lei

Center for Advanced Radiation Sources, The University of Chicago, 5640 S Ellis Avenue, Chicago, IL 60637, USA

E-mail: ninglei@yahoo.com

Received 20 December 2006, in final form 23 March 2007
Published 1 May 2007
Online at stacks.iop.org/JPhysCM/19/216215

Abstract

An approach is proposed to determine the structure of a three-dimensional non-crystalline object from a single two-dimensional x-ray scattering image. If x-ray absorption is ignored, this method, unlike what has been reported in the literature, always generates a structure of real electron density, even in the case that the Ewald sphere curvature is large. In addition, if the original object is thin, the reconstructed object is the integrated electron density of the original one along a path which makes an angle with the incoming x-rays (z-axis) in proportion to the maximum x-ray wavevector transfer magnitude along the axis, revealing the object's depth information. It is demonstrated mathematically that the blurs or ripples associated with a reconstructed object are due to a resolution function effect. Reconstructed structures of a hypothetical three-dimensional object are shown to agree with the theoretical predictions.

(Some figures in this article are in colour only in the electronic version)

1. Introduction

In recent years, there has been intense interest in reconstructing non-periodic two-dimensional 2D) and three-dimensional (3D) objects through their x-ray scattering intensities alone, using dual-space iterative algorithms [1–7]. The importance of these research activities is due to the fact that, unlike electrons, x-rays have large penetration power and are weakly scattered, and therefore a true three-dimensional object can be reconstructed at a spatial resolution limited only by the x-ray wavelength and the sample scattering power. It is expected that, with strong enough incident x-ray intensity, structures of isolated proteins may be obtained [8], and scientists may be able to observe a living cell at work [9].

With an area detector, the x-ray scattering intensity distribution is measured through a series of images corresponding to different sample orientation angles. Nevertheless, due to possible x-ray radiation damage, it may be impossible to obtain more than one image from the

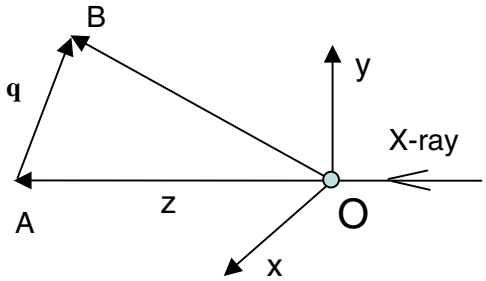

Figure 1. Schematic diagram to show the scattering geometry. The scattering wavevector transfer is indicated by **q**.

same sample. In addition, if the sample structure varies with time, it is extremely desirable to be able to monitor the instantaneous structure without rotating the sample. Therefore, it is very important to know if the structure can be obtained through just one image. If the x-ray wavelength is short enough so that the sample is considered thin, a corresponding 2D object can be reconstructed [10]. 2D structures each determined from a 2D x-ray scattering image of a 3D object at different sample rotation angles were obtained recently by Miao *et al* [11]. In their work, the original object was thin and the Ewald sphere curvature was ignored. Chapman *et al* [10] studied the Ewald sphere curvature effect and concluded that the obtained 2D electron density structure must be, in general, complex since the basic scattering rule for a 2D object, $I(-q_x, -q_y) = I(q_x, q_y)$, is violated, where q_x and q_y are the x-ray wavevector transfers along the x-axis and y-axis, respectively. The complex electron density profile may make explaining the object's structure difficult, and confusion exists in literature as to how to use the obtained complex object to infer the original structure [12].

In this paper, a different approach is developed in section 2 to reconstruct the original object from a single 2D x-ray scattering image. The result shows that the reconstructed electron density under the new approach is not only always positive if ripples are ignored and x-ray absorption is negligible, but also gives information about the relative depth of the components due to Ewald sphere curvature, yielding 3D structural information from 2D scattering data. In section 3, a computer-simulated x-ray scattering experiment on a hypothetical three-sphere structure is carried out to take a 2D x-ray scattering image, and the Fienup hybrid-input–output (HIO) algorithm [13] is used to retrieve the original structure. The retrieved structures are compared to the theory developed in section 2. In section 4, the traditional method to reconstruct the structure (from a single 2D image) is analysed following the insight gained in section 2. A conclusion is given in section 5.

2. Theory

On a single x-ray scattering image, as shown in figure 1, the x-ray wavevector transfer **q** along the z-axis is, assuming that the incoming x-rays are along the positive z-direction, $q_z = -k_0 + \sqrt{k_0^2 - q_x^2 - q_y^2}$, where $k_0 = 2\pi/\lambda = |OA| = |OB|$ and λ is the x-ray wavelength. Therefore, in general, the x-ray scattering structure factor of the object on that image does not satisfy

$$F_0(-q_x, -q_y, q_z) = F_0^*(q_x, q_y, q_z), \tag{1}$$

where the structure factor $F_0(\mathbf{q}) = \int \rho_0(\mathbf{r}) \exp(-\mathrm{i}\mathbf{q}\mathbf{r})\, \mathrm{d}\mathbf{r}$ with $\rho_0(\mathbf{r})$ the object's electron density at location **r**. Nevertheless, modified scattering structure factors can be defined

as

$$F_1(q_x, q_y) = \begin{cases} F_0(q_x, q_y, q_z); & q_y \geqslant 0 \\ F_0^*(-q_x, -q_y, q_z); & q_y \leqslant 0 \end{cases} \tag{2}$$

and

$$F_2(q_x, q_y) = \begin{cases} F_0(q_x, q_y, q_z); & q_y \leqslant 0 \\ F_0^*(-q_x, -q_y, q_z); & q_y \geqslant 0. \end{cases} \tag{3}$$

It is easy to verify that both the modified structure factors $F_1(q_x, q_y)$ and $F_2(q_x, q_y)$ satisfy equation (1). Therefore, we use $|F_1(q_x, q_y)|$ and $|F_2(q_x, q_y)|$ to reconstruct the original object.

We need to investigate theoretically what electron density distributions can be obtained from $|F_1(q_x, q_y)|$ and $|F_2(q_x, q_y)|$. We define projection electron densities $\rho_1(x, y)$ and $\rho_2(x, y)$ in such a way that the modified structure factors $F_1(q_x, q_y)$ and $F_2(q_x, q_y)$ are the Fourier transforms of $\rho_1(x, y)$ and $\rho_2(x, y)$, respectively. Ignoring the Gibbs ripple effect, we have

$$\rho_1(x, y) = \frac{2}{\pi^2} \int \int_{\text{3D object}} \rho_0(x', y', z')\, \mathrm{d}x'\, \mathrm{d}y'\, \mathrm{d}z' \int_0^{q_{xy,\max}} \int_0^{\sqrt{q_{xy,\max}^2 - q_x^2}} \cos[q_x(x' - x - x_0)] \times \cos[q_y(y' - y - y_0) + q_z(z' - z_0)]\, \mathrm{d}q_x\, \mathrm{d}q_y \tag{4}$$

assuming that the detector is round. In equation (4), $q_{xy,\max}$ is the maximum x-ray wavevector transfer in the x–y-plane, and x_0, y_0, and z_0 are translational shift parameters. Similarly,

$$\rho_2(x, y) = \frac{2}{\pi^2} \int \int_{\text{3D object}} \rho_0(x', y', z')\, \mathrm{d}x'\, \mathrm{d}y'\, \mathrm{d}z' \int_0^{q_{xy,\max}} \int_0^{\sqrt{q_{xy,\max}^2 - q_x^2}} \cos[q_x(x' - x - x_0')] \times \cos[q_y(y' - y - y_0') - q_z(z' - z_0')]\, \mathrm{d}q_x\, \mathrm{d}q_y. \tag{5}$$

From equations (4) and (5), it is evident that since the electron density of the original object ρ_0 is real, both the projection electron densities $\rho_1(x, y)$ and $\rho_2(x, y)$ are real.

To continue, we define the following resolution functions

$$H_1(\mathbf{r}) = \int_0^{q_{xy,\max}} \int_0^{\sqrt{q_{xy,\max}^2 - q_x^2}} \cos(q_x x) \cos(q_y y + q_z z)\, \mathrm{d}q_x\, \mathrm{d}q_y, \tag{6}$$

and

$$H_2(\mathbf{r}) = \int_0^{q_{xy,\max}} \int_0^{\sqrt{q_{xy,\max}^2 - q_x^2}} \cos(q_x x) \cos(q_y y - q_z z)\, \mathrm{d}q_x\, \mathrm{d}q_y. \tag{7}$$

Intuitively, if $|q_{xy,\max} x| \gg 1$, due to the oscillation of $\cos(q_x x)$ along the q_x path, both $H_1(\mathbf{r})$ and $H_2(\mathbf{r})$ are small. Similarly, if $|q_{xy,\max} y| \gg 1$, both $H_1(\mathbf{r})$ and $H_2(\mathbf{r})$ are small at $z = 0$. In fact, at $z = 0$, if using a square area detector, the resolution function $H_1(\mathbf{r}) = \sin(q_{x,\max} x) \sin(q_{y,\max} y)(xy)^{-1}$, where $q_{x,\max}$ and $q_{y,\max}$ are the largest wavevector transfers along the x-axis and y-axis, respectively. When $q_{x,\max}$ and $q_{y,\max}$ go to infinity, $H_1(\mathbf{r}) = \pi^2 \delta(x)\delta(y)$. Numerical studies show that, around its central peak, $H_1(\mathbf{r})$ can be approximated by

$$H_1(\mathbf{r}) = \frac{C\, \mathrm{e}^{-(x q_{xy,\max}/\pi)^2 - (y q_{xy,\max}/\pi - z q_{z,\max}/\pi)^2}}{1 + [Q_\perp z/(2\pi \cos\theta)]^2}. \tag{8}$$

In equation (8), $q_{z,\max} = k_0 - \sqrt{k_0^2 - q_{xy,\max}^2}$ is the largest wavevector transfer magnitude along the z-axis, $\tan\theta = q_{z,\max} q_{xy,\max}^{-1}$, C is a constant unrelated to $\mathbf{r}$, and $Q_\perp = q_{xy,\max} \sin\theta +$

$k_0(1-\cos\theta)$. If $\theta \ll 1$, $Q_\perp \approx q_{z,\max}$. Therefore, if $(x'-x-x_0, y'-y-y_0, z'-z_0)$ is not too far from (0, 0, 0), equation (4) becomes

$$\rho_1(x,y) = \frac{2C}{\pi^2}\int\int_{\text{sample}} \rho_0(x',y',z') \times \frac{\mathrm{e}^{-[(x'-x-x_0)q_{xy,\max}/\pi]^2-[(y'-y-y_0)q_{xy,\max}/\pi-(z'-z_0)q_{z,\max}/\pi]^2}}{1+[Q_\perp(z'-z_0)/(2\pi\cos\theta)]^2}\,\mathrm{d}x'\,\mathrm{d}y'\,\mathrm{d}z'. \tag{9}$$

Equation (9) indicates that if the original electron density $\rho_0(\mathbf{r})$ is always positive, then the projection electron density $\rho_1(x, y)$ is also positive. In addition, equation (9) shows that if $Q_\perp$ is small and $q_{xy,\max}$ is large (compared with the inverse of the sample linear size), namely, the sample is thin, $\rho_1(x, y)$ is just the original electron density integrated along the path of

$$\begin{aligned} z'-z_0 &= (y'-y-y_0)q_{xy,\max}/q_{z,\max} \\ x' &= x+x_0. \end{aligned} \tag{10}$$

Similarly, the second projection electron density $\rho_2(x, y)$ is the original electron density integrated along the path of

$$\begin{aligned} z'-z_0' &= -(y'-y-y_0')q_{xy,\max}/q_{z,\max} \\ x' &= x+x_0'. \end{aligned} \tag{11}$$

Therefore, $\rho_1(x, y)$ and $\rho_2(x, y)$ give depth information for the original object. Far away from its central peak, $H_1(\mathbf{r})$ has ripples, both positive and negative, especially when $\mathbf{r}$ is close to the line defined by $z = yq_{xy,\max}/q_{z,\max}(x = 0)$.

3. Computer-simulated experiment and object retrieval

To demonstrate using the proposed modified structure factor amplitudes $|F_1(q_x, q_y)|$ and $|F_2(q_x, q_y)|$ to reconstruct the original object, a computer-simulated experiment is set up. We use an area detector which had 3001 by 3001 number of pixels and an area of 300 mm by 300 mm. X-rays of wavelength of 15 Å were used. The sample–detector distance is 54.6 mm, and the beam stop, with a radius of 0.5 mm, is located 50 mm after the sample. The incoming x-rays are assumed to be polarized along the x-axis and to travel along the z-axis. The sample is composed of three solid spheres of radius R. The spheres have an electron density of one electron per Å^3. The coordinates of the sphere centres are $(3R, 0, 0)$, $(0, 3R, 0)$, and $(0, 0, 3R)$, where R is set at 30 Å. Since the scattering process is a quantum process, the number of scattered x-rays follows a Poisson distribution, and therefore Poisson noises are generated in the data simulation. The scattering intensity is sampled in a grid of 81×81 in reciprocal space at an interval of 0.004 27 Å^{-1} in both q_x and q_y, giving a hypothetical unit cell size of $1470 \times 1470\ \text{Å}^2$. The support is set to be the centre one seventh of the unit cell along each axis. We take $q_{xy,\max} = 0.171\ \text{Å}^{-1}$ which yields $q_{z,\max} = 0.0365\ \text{Å}^{-1}$. Figure 2 shows simulated scattering data which have a *signal-to-noise ratio* (SNR) of 39. The scattering intensities are normalized to one solid radian. Careful examination of the data indicates that the scattering intensities are not centrosymmetric in the q_x–q_y-plane.

We carry out 20 HIO runs on the data and pick the best reconstructed object from the 20 runs with the HIO feedback parameter $\beta_{\text{HIO}} = 1$. We use 800 iterations for each run. There is no non-negative electron density constraint in the HIO procedures. We know that with or without scattering data noise, the reconstructed object may be stable along the iteration path

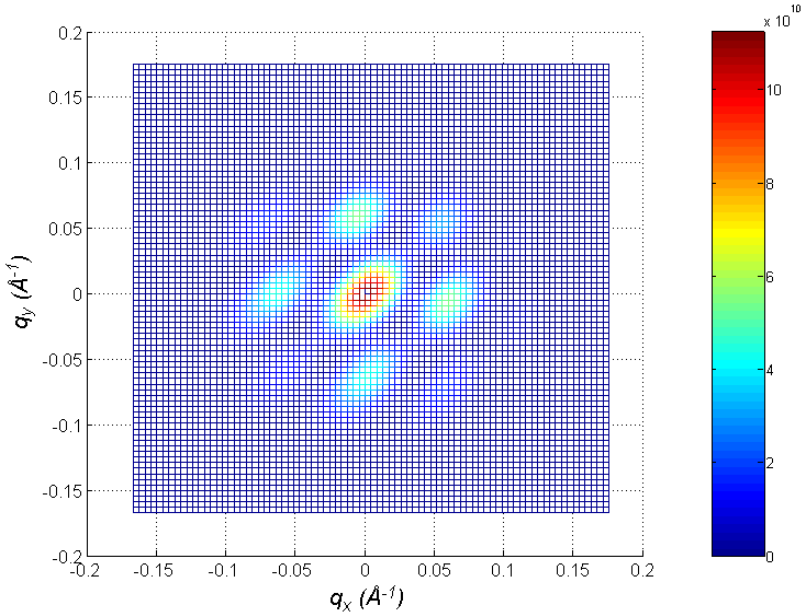

Figure 2. The computer-simulated scattering intensities per solid radian, after dividing the x-ray polarization factors, for the three-solid-sphere object over each of the 81 by 81 grids in reciprocal space. The incoming x-rays were polarized along the x-axis.

but may not be faithful. In order to select the faithfully reconstructed objects, we used the traditional crystallographic R-factor defined as

$$R_{\text{cryst}} = \left(\sum ||F_{\text{HIO}}| - |F_{\text{sim}}||\right) \Big/ \left(\sum |F_{\text{sim}}|\right), \tag{12}$$

and the electron density fluctuation parameter defined as

$$\rho_{\text{fluct}} = \sum_{j=1, j\in S}^{N} \sum_{\substack{4 \text{ nearest} \\ \text{neighbour}}} |\rho_{\text{neighbour}} - \rho_j|/(4N). \tag{13}$$

In equation (12), F_{HIO} and F_{sim} are the structure factors obtained from the HIO procedure and the simulated experiment, respectively. Note that in equation (12), in calculating F_{HIO}, the electron density is set to zero outside the support. In equation (13), ρ_j is the electron density at grid j on the support S, and N is total number of grids on the support (strictly speaking, j does not go to the border of the support and N is the total number of grids on the support minus the number of grids on the support border). In addition, we define a parameter to balance the measures provided by R_{cryst} and ρ_{fluct},

$$\eta = \frac{\langle R_{\text{cryst}}\rangle - R_{\text{cryst}}}{\langle R_{\text{cryst}}\rangle} + \frac{\langle \rho_{\text{fluct}}\rangle - \rho_{\text{fluct}}}{\langle \rho_{\text{fluct}}\rangle}, \tag{14}$$

where $\langle\cdots\rangle$ indicates the averages of the results from the 20 HIO runs. We picked the reconstructed objects using the following criteria: (1) $R_{\text{cryst}} < \langle R_{\text{cryst}}\rangle$, (2) $\rho_{\text{fluct}} < \langle \rho_{\text{fluct}}\rangle$, and (3) η is among the largest. We show, in figure 3(a), a reconstructed projection electron density from $|F_1|$. The reconstructed object has the largest η among the 20 HIO runs. The object has $R_{\text{cryst}} = 0.068$, $\rho_{\text{fluct}} = 4.3$ Å^{-2}, and $\eta = 0.23$. We carried out another 20

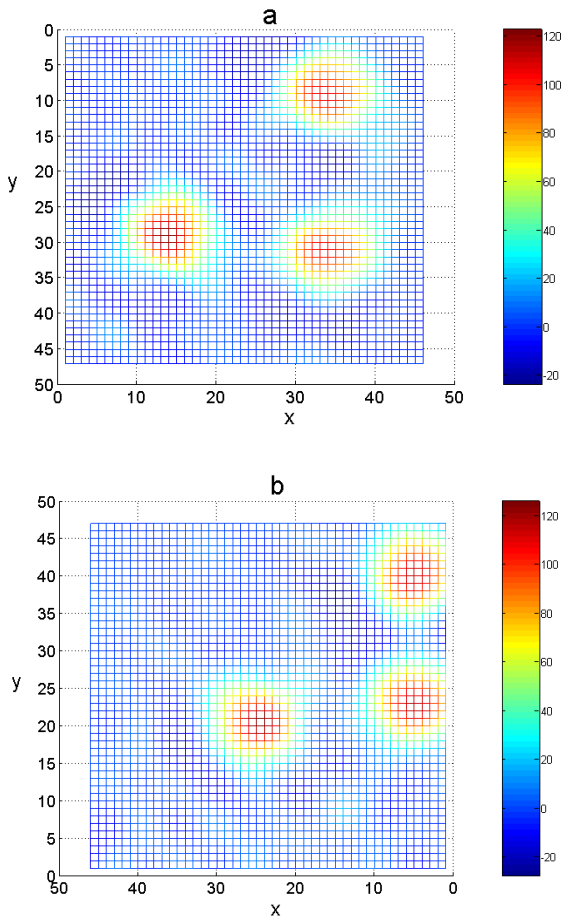

Figure 3. HIO procedure reconstructed 2D objects from a single 2D x-ray scattering image on a three-sphere object with the structure factor amplitudes constructed according to (a) equation (2), and (b) equation (3). The spheres are located at (90 Å, 0, 0), (0, 90 Å, 0), and (0, 0, 90 Å). Each grid step represents 4.54 Å. There is no non-negative constraint in the HIO procedures. The HIO obtained parameters are: (a) $R_{\text{cryst}} = 0.068$, $\rho_{\text{fluct}} = 4.3$ Å^{-3}, and $\eta = 0.23$. (b) $R_{\text{cryst}} = 0.061$, $\rho_{\text{fluct}} = 3.7$ Å^{-2}, and $\eta = 0.43$.

HIO runs, using $|F_2|$, and we show a plot of the best reconstructed object in figure 3(b) ($R_{\text{cryst}} = 0.061$, $\rho_{\text{fluct}} = 3.7$ Å^{-2}, $\eta = 0.43$). In figures 3(a) and (b), the original grid is divided into four equally spaced smaller grids along each axis, and therefore each grid step in the figures represents 4.54 Å. The figures show that the reconstructed objects resemble the original one, but with a slight relative move along the y-axis for the bottom right component, indicating that the component does not have the same location along the z-axis as the other two. For the bottom right component, between its locations in figures 3(a) and (b), it moves about 6.5 ± 1 steps along the y-axis, namely, 29.5 ± 4.5 Å, relative to the other two. Using equations (10) and (11), we obtain that the difference in the locations along the z-axis is 69 ± 11 Å, which is not that far from the real difference of 90 Å. A more accurate value can be achieved through sampling the data up to a higher wavevector transfer. This simple example shows that not only is the reconstructed electron density profile all positive (or all negative), given that the original electron density is

positive, but also that the method provides a way to obtain component locations along the z-axis, in addition to their x–y locations. The accuracy in the z-axis location determination is proportional to $q_{xy,\max}^{-1} q_{z,\max}$.

What happens to the reconstructed object if the sphere originally located at $(0, 0, 3R)$ is relocated to $(0, 0, L)$ with $L > 2\pi/q_{z,\max} = 172$ Å for $q_{z,\max} = 0.0365$ Å^{-1}? This is the case when the object is thick. Let us set $L = 400$ Å and make 20 HIO runs to reconstruct $\rho_1(x, y)$, with the same HIO related parameter values as those for figures 3(a) and (b), except that the support is set at the centre one third of the hypothetical unit cell along each coordinate. The scattering data has an SNR of 38. The results reveal that if there is no non-negative electron density constraint, R_{cryst} is quite small, with a mean of 0.082 and a standard deviation of 0.0041. Since L is large, no matter what the shift z_0 is, at least one of the spheres is at the resolution function tail over which equation (8) is invalid and a resolution function ripple effect occurs. The ripples can be both positive and negative, and therefore, the reconstructed object contains both positive and negative electron densities. We pick, out of the 20 runs, the one with the largest η and show the reconstructed object in figure 4(a) which has $\eta = 0.13$, $R_{\text{cryst}} = 0.076$, and $\rho_{\text{fluct}} = 1.6$ Å^{-2}. Note that most results from the 20 HIO runs do not resemble the original object at all, although their R_{cryst} are quite small. Now we enforce the non-negative electron density constraint. We have found that R_{cryst} becomes much larger and has a mean of 0.32 and a standard deviation of 0.019. Most of the reconstructed objects, however, do show recognizable spheres, such as that shown in figure 4(b), which has $R_{\text{cryst}} = 0.31$, $\rho_{\text{fluct}} = 1.3$ Å^{-2}, and $\eta = 0.14$. In figure 4(b), as expected, the lower right component not only moves downwards along the y-axis, but also to the left slightly, agreeing with the resolution function behaviour at its tail revealed by numerical computation on equation (6). Note that the much smaller ρ_{fluct} in figures 4(a) and (b) than those in figures 3(a) and (b) are primarily due to the difference in the support region sizes.

4. Analysis of traditional approach

Follow the analysis developed in section 2, for the traditional approach, the responsible electron density for the measured scattering intensity is

$$\rho(x, y) = \frac{1}{\pi^2} \int \int_{\text{3D object}} \rho_0(x', y', z')\, \mathrm{d}x'\, \mathrm{d}y'\, \mathrm{d}z' H_{\text{T}}(x' - x - x_0'', y' - y - y_0'', z' - z_0''), \tag{15}$$

where the complex resolution function is defined as

$$H_{\text{T}}(\mathbf{r}) = \int_0^{q_{xy,\max}} \int_0^{\sqrt{q_{xy,\max}^2 - q_x^2}} \cos(q_x x) \cos(q_y y) \mathrm{e}^{-\mathrm{i}q_z z}\, \mathrm{d}q_x\, \mathrm{d}q_y. \tag{16}$$

In equation (15), x_0'', y_0'', and z_0'' are object translational shift parameters. When around its major peaks, our numerical calculations show that the complex resolution function can be approximated by

$$H_{\text{T}}(\mathbf{r}) = \mathrm{e}^{-(x^2+y^2)q_{xy,\max}^2/c_0^2} [C_{T,R} \mathrm{e}^{-(zq_{z,\max}/c_1)^2} - \mathrm{i} C_{T,I} \sin(c_2 z q_{z,\max})], \tag{17}$$

where $C_{T,R} = \pi q_{xy,\max}^2/4$, $C_{T,I} = \pi q_{z,\max}(k_0 - 2q_{z,\max}/3)/(4c_2)$, $c_0 = 2.7$, $c_1 = 2.4$, and $c_2 = 0.61$. Therefore the real and imaginary parts of the electron density are

$$\rho_R(x, y) = \frac{C_{T,R}}{\pi^2} \int \int_{\text{3d object}} \rho_0(x', y', z')\, \mathrm{d}x'\, \mathrm{d}y'\, \mathrm{d}z' \mathrm{e}^{-(x^2+y^2)q_{xy,\max}^2/c_0^2 - (zq_{z,\max}/c_1)^2}, \tag{18}$$

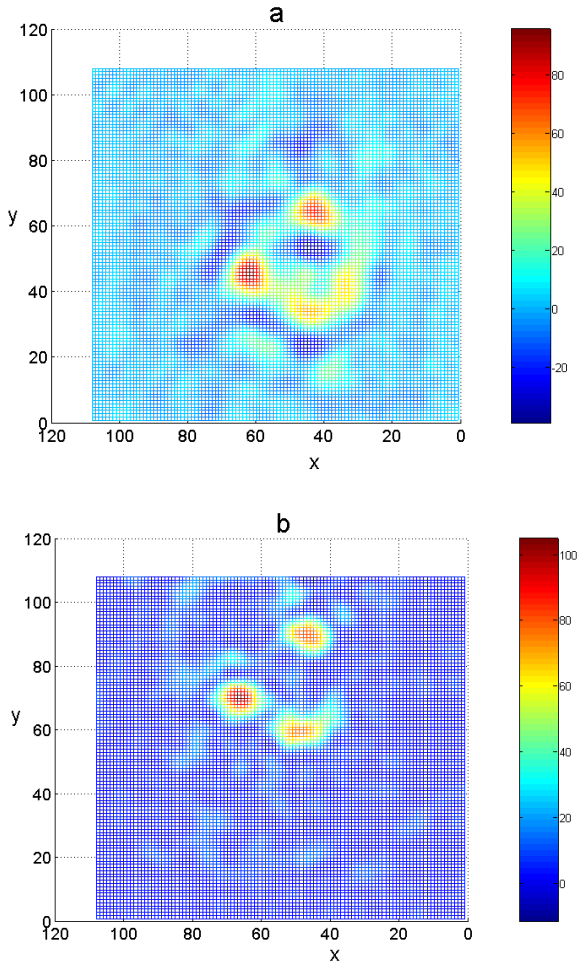

Figure 4. HIO procedure reconstructed 2D objects from a single 2D x-ray scattering image on a three-sphere object with the structure factor amplitudes constructed according to equation (2). The spheres are located at (90 Å, 0, 0), (0, 90 Å, 0), and (0, 0, 400 Å). Each grid step represents 4.54 Å. (a) No non-negative electron density constraint. $\eta = 0.13$, $R_{\text{cryst}} = 0.076$, and $\rho_{\text{fluct}} = 1.6$ Å^{-2}. (b) With non-negative electron density constraint. $R_{\text{cryst}} = 0.31$, $\rho_{\text{fluct}} = 1.3$ Å^{-2}, and $\eta = 0.14$.

and

$$\rho_I(x, y) = \frac{C_{T,I}}{\pi^2} \int\int_{\text{3D object}} \rho_0(x', y', z')\, \mathrm{d}x'\, \mathrm{d}y'\, \mathrm{d}z' \mathrm{e}^{-(x^2+y^2)q_{xy,\max}^2/c_0^2} \sin(c_2 z q_{z,\max}). \tag{19}$$

Note that if $q_{z,\max} q_{xy,\max}^{-1}$ is not large, the half-width at half-maximum (HWHM) for $H_1(\mathbf{r})$ along the z-axis around its main peak is about $2\pi q_{z,\max}^{-1}$, as shown in equation (8). The real part of the electron density $\rho_R(x, y)$ is the integral of the original object's electron density along a line which is parallel to the z-axis. However, the HWHM for the real part of the complex resolution function $H_{\text{T}}(\mathbf{r})$ along the z-axis is only 2.4 $q_{z,\max}^{-1}$, significantly smaller than $2\pi q_{z,\max}^{-1}$. Therefore, even if the original object can be considered thin under the method proposed in section 2, it may be too thick for the traditional method using the real part of the reconstructed structure. To prove our understanding, we carry out ten HIO runs on the scattering

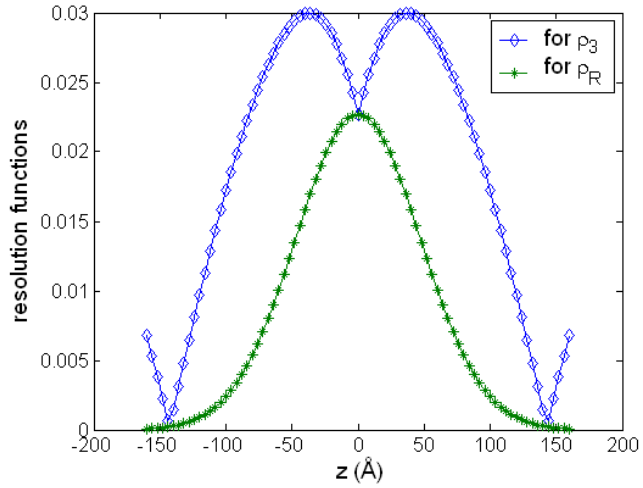

Figure 5. Plots of the resolution functions associated with $\rho_R(x, y)$ and $\rho_3(x, y)$, along the z-axis. $q_{z,\max} = 0.036$ Å^{-1}, $q_{xy,\max} = 0.17$ Å^{-1}, and the x-ray wavelength is 15 Å.

intensity from a single x-ray scattering image on the three-solid-sphere object described in section 3, without scattering noise. The spheres are located at $(3R, 0, 0)$, $(0, 0, 3R)$, and $(0, 0, 3R)$, with the radius R set at 30 Å. The HIO related parameter values and measurement grid sizes and numbers are the same as those in section 3. The x-ray wavelength is 15 Å and the simulated experiment setup is the same as that described in section 3. In seven out of the ten runs, the real parts give blurred images for the sphere located at $(0, 0, 3R)$, indicating that the original object is too thick. Indeed, since $q_{z,\max} = 0.0365$ Å^{-1}, $c_1 q_{z,\max}^{-1} = 65.8$ Å, which is less than the object thickness of about 90 Å $+ 2R$. For comparison, we carry out ten HIO runs with the modified structure factor $F_1(q_x, q_y)$ proposed in section 2, using the same simulated scattering data. All of the reconstructed objects are clear, without much blur, indicating that the object was thin. Furthermore, we can see from equations (18) and (19) that the modulus of the complex electron density $\rho(x, y)$ may give a false structure even if the original electron density is of the same sign. Moreover, if the scattering length can be both positive and negative, as in the cases of neutron scattering and the non-Bragg scattering from substitution disorder in a crystal [14], the modulus does not predict the original structure faithfully.

What may be more useful is to use

$$\rho_3(x, y) = |\rho_R(x, y)| + |\rho_I(x, y)|, \tag{20}$$

to infer the original structure, in the case that the scattering length is of the same sign, although there is no depth information gained. From equations (18) and (19), we have

$$\rho_3(x, y) = \frac{1}{\pi^2} \int \int_{\text{3D object}} \rho_0(x', y', z')\, \mathrm{d}x'\, \mathrm{d}y'\, \mathrm{d}z' \mathrm{e}^{-(x^2+y^2)q_{xy,\max}^2/c_0^2} \times [C_{T,R} \mathrm{e}^{-(zq_{z,\max}/c_1)^2} + C_{T,I} |\sin(c_2 z q_{z,\max})|]. \tag{21}$$

We plot, in figure 5, the resolution functions along the z-axis associated with $\rho_R(x, y)$ and $\rho_3(x, y)$. In the figure, we use $q_{z,\max} = 0.036$ Å^{-1}, $q_{xy,\max} = 0.17$ Å^{-1}, and an x-ray wavelength of 15 Å. The resolution function along the z-axis associated for $\rho_3(x, y)$ has an HWHM of $1.37\pi q_{z,\max}^{-1}$, which is much larger than that associated with $\rho_R(x, y)$.

5. Conclusion

In this paper we have suggested a way to determine the structure of a 3D object from its 2D x-ray scattering image even when the Ewald curvature is large. We showed mathematically that under the method proposed in section 2, the reconstructed object is the original one convoluted with a real resolution function. When the object is thin, the reconstructed electron density is the original one integrated along a path which makes an angle with the incoming x-rays described by equation (10) or (11). We showed that the relative move of a component, in the reconstructed projection electron density profiles ρ_1 and ρ_2 which correspond to, respectively, using the upper and lower half planes of the scattering data, gives the information about its relative location along the z-axis. Reconstructed objects from data collected from computer-simulated experiments on a three-uniform-sphere sample were shown to agree with our understanding. In addition, we analysed the traditional reconstruction method and reached the conclusion that, with Ewald sphere curvature effects, the real part of the reconstructed complex electron density allows a sample thickness much smaller than that allowed from the method we proposed in this paper.

References

[1] Miao J, Charalambous P, Kirz J and Sayre D 1999 *Nature* **400** 342
[2] Miao J, Ishikawa T, Johnson B, Anderson E H, Lai B and Hodgson K O 2002 *Phys. Rev. Lett.* **89** 088303
[3] Marchesini S, He H, Chapman H N, Hau-Riege S P, Noy A, Howells M R, Weierstall U and Spence J C H 2003 *Phys. Rev.* B **68** 140101(R)
[4] He H, Marchesini S, Howells M, Weierstall U, Chapman H, Hau-Riege S, Noy A and Spence J C H 2003 *Phys. Rev.* B **67** 174114
[5] Thilbault P, Elser V, Jacobsen C, Shapiro D and Sayre D 2006 *Acta Crystallogr.* A **62** 248
[6] Pfeifer M, Williams G J, Vartanyants I A, Harder R and Robinson I K 2006 *Nature* **442** 63
[7] Shapiro D, Thibault P, Beetz T, Elser V, Howells M, Jacobsen C, Kirz J, Lima E, Miao H, Neiman A M and Sayre D 2005 *Proc. Natl Acad. Sci. USA* **102** 15343
[8] Spence J C H, Schmidt K, Wu J S, Hembree G, Weierstall U, Doak B and Fromme P 2005 *Acta Crystallogr.* A **61** 237
[9] Miao J, Hodgson K O, Ishikawa T, Larabell C A and LeGros M A 2003 *Proc. Natl Acad. Sci. USA* **100** 110
[10] Chapman H N, Barty A, Marchesini S, Noy A, Hau-Riege S P, Cui C, Howells M, Rosen R, He H, Spence J C H, Weierstall U, Beetz T, Jacobsen C and Shapiro D 2006 *Opt. Soc. Am.* A **23** 1179
[11] Maio J, Nishino Y, Kohmura Y, Johnson B, Song C, Risbud S H and Ishikawa T 2005 *Phys. Rev. Lett.* **95** 085503
[12] Spence J C H, Weierstall U and Howells M 2002 *Phil. Trans. R. Soc.* A **360** 875
[13] Fienup J R 1982 *Appl. Opt.* **21** 2758
[14] Warren B E 1990 *X-ray Diffraction* (New York: Dover)